Photochemical & Photobiological Sciences (2024) 23:451–462
https://doi.org/10.1007/s43630-023-00530-1

ORIGINAL PAPERS

Solvent and alkyl substitution effects on charge-transfer mediated triplet state generation in BODIPY dyads: a combined computational and experimental study

Yasi Dai[1,2] · Angela Dellai[1] · Elena Bassan[1,2] · Caterina Bellatreccia[1,2] · Andrea Gualandi[1,2] · Michele Anselmi[1] · Pier Giorgio Cozzi[1,2] · Paola Ceroni[1,2] · Fabrizia Negri[1,2,3]

Received: 30 August 2023 / Accepted: 21 December 2023 / Published online: 7 February 2024

Abstract

Donor–acceptor dyads based on BODIPYs have been recently employed to enhance the formation of triplet excited states with the process of spin–orbit charge transfer intersystem crossing (SOCT-ISC) which does not require introduction of transition metals or other heavy atoms into the molecule. In this work we compare two donor–acceptor dyads based on *meso*-naphthalenyl BODIPY by combining experimental and computational investigations. The photophysical and electrochemical characterization reveals a significant effect of alkylation of the BODIPY core, disfavoring the SOCT-ISC mechanism for the ethylated BODIPY dyad. This is complemented with a computational investigation carried out to rationalize the influence of ethyl substituents and solvent effects on the electronic structure and efficiency of triplet state population via charge recombination (CR) from the photoinduced electron transfer (PeT) generated charge-transfer (CT) state. Time dependent-density functional theory (TD-DFT) calculations including solvent effects and spin–orbit coupling (SOC) calculations uncover the combined role played by solvent and alkyl substitution on the lateral positions of BODIPY.

Graphical abstract

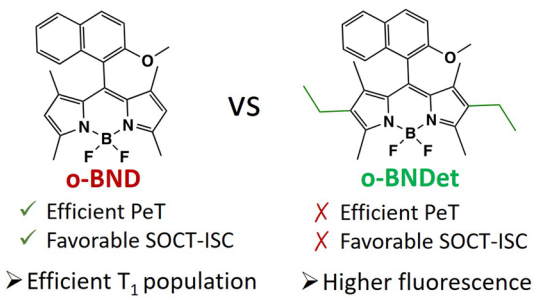

Keywords State specific solvent effects · Phosphorescence · Triplet state · DFT · TD-DFT · Spin–orbit coupling calculations · BODIPY

Special issue entitled "Probing, structuring and moving molecular matter with light" in honor of Prof. Fred Brower.

✉ Paola Ceroni
paola.ceroni@unibo.it

✉ Fabrizia Negri
fabrizia.negri@unibo.it

[1] Department of Chemistry Giacomo Ciamician, University of Bologna, Bologna, Italy

[2] Center for Chemical Catalysis-C3, Alma Mater Studiorum-Università di Bologna, Via Selmi 2, 40126 Bologna, Italy

[3] INSTM, UdR Bologna, Via F. Selmi, 2, 40126 Bologna, Italy

1 Introduction

The efficient formation of long-lived triplet excited states is essential for several applications such as photoredox catalysis [1–3], photodynamic therapy (PDT) [4–6] and triplet–triplet annihilation up-conversion [7–9].

Although boron dipyrromethene (BODIPY) derivatives display efficient fluorescence, in recent years, judicious modifications of the BODIPY skeleton have been proposed to obtain efficient triplet state populations by enhancing the non-radiative decay to the triplet state [10]. This result can be obtained by introducing heavy atoms [11, 12], by coupling BODIPY to electron donating chromophores in donor–acceptor (DA) dyads [13–15], by linking BODIPY to radical species (e.g., 2,2,6,6-tetramethylpiperidine 1-oxyl, TEMPO) [16] or by exploiting covalently-linked BODIPY dimers [17, 18]. In the last two cases, the population of the T_1 excited state is mediated by a photoinduced electron transfer (PeT) process [19] leading to a charge transfer (CT) state. The long-lived triplet excited state may then be involved in bimolecular sensitization processes, e.g. production of singlet oxygen used in photocatalysis and photodynamic therapy [5, 13, 20].

CT-mediated triplet state generation has been observed not only in donor–acceptor (DA) dyads based on BODIPYs [21–28], but also for several other organic chromophores [29–33]. According to this process, the photo-generated CT state can undergo two further processes: a non-radiative charge recombination (CR) into the ground state (CR_{GR}) or into the lowest triplet excited state (CR_T) via spin–orbit charge transfer intersystem crossing (SOCT-ISC). Recent investigations on a library of BODIPY dyads have shown that high yields of triplet state formation are observed when the CT state lies close in energy to the lowest singlet excited state (S_1). In this case, the CR_{GR} process falls within the Marcus inverted region [34] and is relatively slow due to a large negative value of the free energy change associated to the process. Under such conditions, the CR_T process can become considerably faster due to a smaller energy gap between the CT state and the lowest triplet excited state (T_1) [24].

The rate constants associated with the PeT and CR steps can be modulated by varying the number of alkyl substituents in BODIPY dyads, thereby tuning the reduction potentials of the BODIPY core [35]. Since the energy of the CT state is strongly affected by the polarity of the environment, the efficiency of triplet state formation by SOCT-ISC is also expected to be solvent dependent.

With the above concepts in mind, this work focuses on two BODIPY dyads, **o-BND** and **o-BNDet** (Fig. 1), featuring an orthogonally-oriented electron donating moiety, 2-methoxynaphthalene, covalently linked in the *meso* position. The design is such that (Fig. 2), upon excitation of the BODIPY core a PeT from the donor to the BODIPY unit takes place, leading to the population of a CT singlet excited state (^{1}CT). This decays by CR to form the T_1 state localized on the BODIPY unit. Very recently **o-BND** was used for the first time in metallaphotoredox catalysis [13]. Here we expand the study by exploring how the ethyl substituted BODIPY core and solvent effects impact the population of the lowest triplet excited state. These effects are investigated by combining photophysical, electrochemical and computational studies. The relative order of the low-lying excited states plays a crucial role in both the PeT and the CR processes, and is strongly influenced by substitution, as well as solvent effects. For this reason, we determined excited state optimized geometries with time-dependent density functional theory (TD-DFT) calculations and explore solvent effects in the framework of the polarizable continuum model (PCM) [36] using different

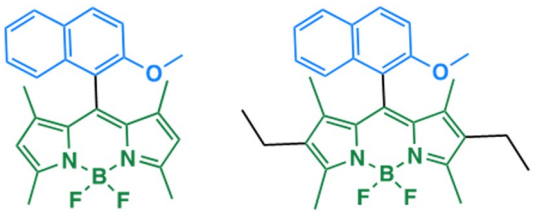

Fig. 1 Structure of the studied dyads: (left) **o-BND** and (right) **o-BNDet**

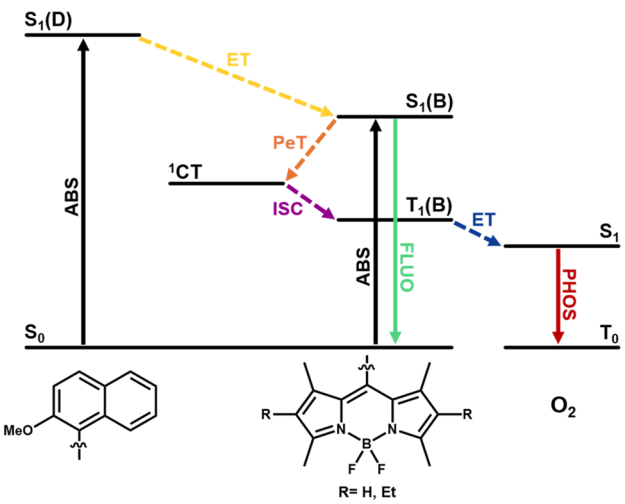

Fig. 2 Jablonski diagram illustrating the main energy levels and deactivation pathways for CT-mediated triplet state generation in BODIPY derivatives. The local excitation nature of the excited states schematically depicted in the diagram is indicated in parenthesis (D for the donor, B for BODIPY). *ET* energy transfer, *PeT* photoinduced electron transfer, *ISC* intersystem crossing, *ABS* absorption, *FLUO* fluorescence, *PHOS* phosphorescence. The production of singlet oxygen by sensitization is also indicated in the diagram

available correction schemes: the standard linear response (LR), the corrected linear response (cLR) [37, 38] and the recently proposed cLR^2 schemes [39]. Finally, spin–orbit couplings (SOCs), which crucially influence the efficiency of the CR_T and CR_{GR} processes, are computed to rationalize the observed differences.

2 Experimental and computational details

2.1 Photophysical and electrochemical characterization

Photophysical measurements were carried out in acetonitrile at room temperature. UV–vis absorption spectra were recorded with a PerkinElmer λ40 spectrophotometer using quartz cells with path length of 1.0 cm. Emission spectra were acquired with either a Perkin Elmer LS55 spectrofluorometer, equipped with a Hamamatsu R928 phototube, or an Edinburgh FLS920 spectrofluorometer. Excitation spectra in the visible range were acquired with the fluorimeter Perkin-Elmer LS55. Emission quantum yields were measured following the method of Demas and Crosby [40]. Standard used: fluoresceine in NaOH 0.1 M ($\Phi_{FLUO} = 95\%$) [41]. Singlet oxygen emission was measured using Edinburgh FLS920 spectrofluorometer equipped with a liquid nitrogen cooled ultrapure germanium crystal as a detector. The quantum yield of population of the luminescent singlet excited state of dioxygen (Φ_Δ) was evaluated by comparison of luminescence intensity of $^1O_2$ at 1270 nm of the sample of interest and of $[Ru(bpy)_3]^{2+}$ standard ($\Phi_\Delta = 57\%$) [42], recorded for isoabsorbing acetonitrile solutions at the excitation wavelength [43]. Emission intensity decays were measured by the above-mentioned Edinburgh FLS920 spectrofluorometer equipped with a TCC900 card for data acquisition in time-correlated single-photon counting experiments (0.5 ns time resolution) with a 405 nm laser. The estimated experimental errors are: 2 nm on the absorption and emission band maximum, 5% on the molar absorption coefficient and luminescence lifetime, and 10% on the luminescence and photoisomerization quantum yields.

Electrochemical experiments were carried out in argon-purged acetonitrile at room temperature with an EcoChemie Autolab 30 multipurpose instrument interfaced to a personal computer. The working electrode was a glassy carbon electrode (0.08 cm^2, Amel); the counter electrode was a Pt spiral and a silver wire was employed as a quasi-reference electrode (QRE). The potentials reported are referred to SCE by measuring the potential with respect to ferrocene (+ 0.39 V vs. SCE in acetonitrile). The substrate concentrations were in the mM range and the supporting electrolyte ($TEAPF_6$) was 0.1 M. The errors on the redox potential values are estimated to be ± 10 mV for reversible processes and ± 20 mV for irreversible processes.

2.2 Computational details

Ground state equilibrium structures of the two dyads shown in Fig. 1 were determined with DFT calculations using the M06-2X functional with the 6-311G* basis set (Figures S1–S2). Solvent effects (MeCN and, for selected computations, n-Hexane) were included with the PCM [36]. All the reported optimized geometries correspond to minima as verified by vibrational frequency calculations.

Excited state wavefunctions and excitation energies were calculated with TD-DFT, using the M06-2X functional and the 6-311G* basis set. Generally, ten triplet and ten singlet excited states were included in the calculations. Due to the constrained cyanine nature of BODIPY and the generally insufficient electron correlation at TD-DFT level, excitation energies are systematically overestimated by ca. 0.4–0.5 eV [44–47] at this level of theory. Nevertheless, several benchmark works have demonstrated that the M06-2X functional is suitable to describe the variations induced by side groups, modifications of the skeleton, stiffening or extension of the conjugated path on excitation energies of BODIPY derivatives [47–50].

Solvent polarization effects on excitation energies in solution were determined with the use of the standard linear response (LR), with the state specific (SS) corrected linear response (cLR) [37, 38] and with the cLR^2 approach [39] (see the supporting information for additional details). The LR and SS approaches can be used to compute corrected excitation energies, either equilibrating the fast or the complete solvent degrees of freedom on the ground and excited states, such as to include the effect of solvent reorganization energy on absorption or emission processes. Only the fast solvent component was equilibrated (hereafter indicated as NEQ) in calculations of excited state energies used to model absorption spectra, while a fully equilibrated solvent was assumed (hereafter labelled EQ) for excited state energies employed in the discussion of photo-deactivation processes. Accordingly, the solvent correction included in excited state calculations is indicated by the label LR_{NEQ}, LR_{EQ}, cLR_{NEQ}, cLR_{EQ}, cLR_{NEQ}^2, cLR_{EQ}^2.

Excited state geometry optimizations were carried out at TD-M06-2X/6-311G* level of theory including solvent corrections with the LR approach. The optimization of the S_1 state localized on the BODIPY moiety was readily obtained for both dyads (Figure S3). Hereafter, such state as well as the state T_1 bearing the same BODIPY localized excitation nature, will be labelled as $S_1(B)$ and $T_1(B)$, as done in Fig. 2. We also carried out geometry optimization for the CT states, conscious that for such states the LR approach may

be inaccurate for large electron–hole separations [51]. The LR method is indeed well suited for electronic excitations characterized by small changes of electron density as is the case for the BODIPY localized S_1(B) state. One of the major limits of the LR approach is that solvent stabilization is proportional to the transition dipole moment. Thus, because of its smaller transition dipole moment, the stabilization of the ^{1}CT state is always underestimated. Such over stabilization of the S_1(B) state prevented the optimization of the ^{1}CT state for **o-BND** because during its geometry optimization, whenever it became closer to the BODIPY localized S_1(B) state, a larger erroneous stabilization of the latter led to an inversion of states. In contrast, for **o-BNDet** the ^{1}CT optimized geometry was determined (Figure S4), owing to its higher energy compared to the BODIPY localized S_1(B) state. Nevertheless, for both dyads we were able to obtain the equilibrium geometry of the ^{3}CT state (Figure S5), which shares a similar wavefunction with ^{1}CT. The geometries of the ^{3}CT and ^{1}CT states of **o-BNDet** display modest differences (Figure S6) and therefore the former can be assumed as representative of the ^{1}CT equilibrium structure of **o-BND**. Hereafter, both ^{3}CT and ^{1}CT structures will be considered for the SOC calculations (see below).

The intra-molecular reorganization energies λ_i associated with the $S_1(B) \rightarrow {}^1CT$, $^1CT \rightarrow S_0$ (CR_{GR}) and $^1CT \rightarrow T_1(B)$ (CR_T) photo-induced processes, were determined for **o-BNDet** with the four points adiabatic potential approach [52], using in vacuo optimized geometries (see Figure S7). For highly polar solvents, equilibrium and non-equilibrium regimes represent very different solvent configurations and their energy difference is generally known as solvent reorganization energy λ_s [37]. To separate the solvent reorganization energy from the total reorganization energy, and to gain insight on the magnitude of the solvent reorganization at different geometries, we performed the complete absorption (non-equilibrium regime) / emission (equilibrium regime) cycle by keeping the molecular geometry frozen at each optimized molecular structure (ground and excited states) and extracted the values of solvent reorganization with the four points adiabatic potential approach (Figure S8). All calculations were performed with the Gaussian 16 package [53].

SOC calculations were carried out at the ground state and CT state geometries optimized in MeCN. The SOC integrals were calculated with the spin–orbit mean-field (SOMF) method, with one-center approximation applied to the exchange term, (SOMF(1X)) [54, 55]. Relativistic corrections were included with the zeroth order regular approximation (ZORA) [56] using the basis sets specifically designed for these all-electrons calculations ZORA-def2-TZVP. The calculations were carried out with ORCA 5.0.1 package [57] with the Tamm-Dancoff approximation (TDA) [58].

Table 1 Redox potentials of the studied compounds in degassed MeCN, in V vs. SCE

Molecule	$E(B/B^{\cdot-})$	$E(B^{\cdot+}/B)$
o-BND	− 1.15	+ 1.15
o-BNDet	− 1.24	+ 1.02

3 Results and discussion

3.1 Electrochemical characterization

Electrochemical characterization was performed by cyclic voltammetry in degassed MeCN solution (Table 1 and Figure S9). The observed electron transfer processes are chemically and electrochemically reversible for both compounds. The processes reported in Table 1 are likely located on the BODIPY core, as suggested by the more positive and chemically-irreversible electron transfer process observed for the oxidation of 2-methoxynaphthalene[41] and by the similarity of redox potentials with literature values for BODIPY dyes [35]. This result indicates that the BODIPY and naphthalene units are electronically decoupled.

It is worth noting that **o-BNDet** displays oxidation and reduction processes cathodically shifted (ca. 100 mV) compared to those observed for **o-BND**. The cathodic shift is correlated to the ethyl substitution that increases the electron density on the core, as previously reported [35].

3.2 Photophysical characterization

o-BND and **o-BNDet**'s photophysical properties in MeCN were compared in order to understand the effect of alkylation of the BODIPY core (Table 2). **o-BND**'s absorption spectrum is characterized by a slightly vibrationally-structured band at 502 nm, which is typical of the $S_0 \rightarrow S_1$(B) electronic transition in BODIPY derivatives. Moreover, its fluorescence spectrum is specular to the lowest absorption band and the small Stokes shift (13 nm) suggests a small geometrical distortion of the S_1(B) and S_0 states. Similar remarks can be drawn by observing **o-BNDet**'s absorption and emission spectra, although a bathochromic shift is present in the latter (Fig. 3), as explained by computational results (vide infra). Besides, we observed a slightly longer lifetime for **o-BNDet** compared to **o-BND** (Table 2) and a significantly higher fluorescence quantum yield of **o-BNDet** compared to **o-BND** (60%). Based on these values, we calculated the fluorescence decay constants (k_{FLUO}) and the non-radiative decay constants (k_{nr}), i.e. the sum of the rate constants of non-radiative processes deactivating the S_1(B) state of the BODIPY core, namely internal conversion $S_1(B) \rightarrow S_0$, inter system crossing $S_1(B) \rightarrow T_1(B)$ and photoinduced electron transfer $S_1(B) \rightarrow {}^1CT$ (Table 2). k_{FLUO} is very similar for the two dyes, while a sixfold reduction of

Table 2 Photophysical properties of the studied compounds in air-equilibrated MeCN

Molecule	$\lambda_{max\ ABS}$ (nm)	$\lambda_{max\ FLUO}$ (nm)	τ_{FLUO} (ns)	Φ_{FLUO}	k_{FLUO} (10^8 s^{-1})	k_{nr} (10^7 s^{-1})[a]	Φ_Δ
o-BND	502	515	5.9	60%	1.0	6.7	27%
o-BNDet	525	543	7.0	91%	1.3	1.3	n.d.

n.d. not detected

[a]k_{nr} is the sum of all the non-radiative processes deactivating the S_1 excited state, namely the internal conversion $S_1(B) \rightarrow S_0$ and the inter system crossing $S_1(B) \rightarrow T_1(B)$

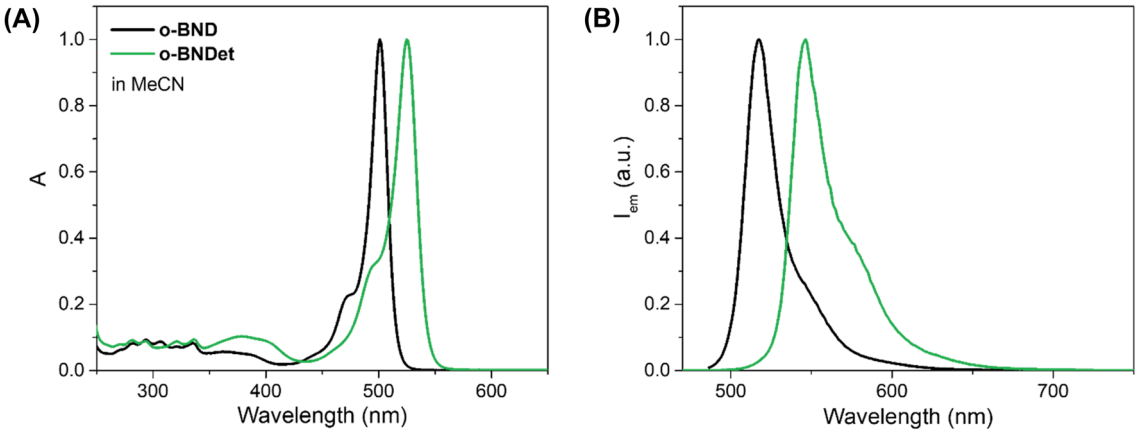

Fig. 3 Normalised absorption (**A**) and emission (**B**) spectra of **o-BND** (black; λ_{EXC}: 480 nm) and **o-BNDet** (green; λ_{EXC}: 450 nm) in air-equilibrated MeCN at room temperature

k_{nr} is observed for **o-BNDet** compared to **o-BND**. Indeed, as previously discussed the addition of ethyl groups on the BODIPY skeleton cathodically shifts the reduction potential of the BODIPY core. As a result, the photoinduced electron transfer from 2-methoxynaphthalene to the BODIPY core is less favoured and fluorescence becomes the predominant deactivation pathway of the S_1(B) excited state. In a parallel manner, the quantum yield for the generation of singlet oxygen is 27% in the case of **o-BND** (Figure S10) and negligible for **o-BNDet**. Population of the luminescent singlet excited state of dioxygen dissolved in solution occurs via energy transfer by the lowest T_1(B) state of **o-BND**, therefore indicating that the CT-state-mediated mechanism that leads to the population of T_1(B) is viable in this derivative (see introduction and Fig. 2), but not in the case of **o-BNDet**.

3.3 Modeling photophysical properties of BODIPY dyads

To assist the interpretation of experimental data and, specifically, to assess the effect of solvent and ethyl substitution on the sequence of photoinduced events, we investigated the two BODIPY dyads in their ground and excited states.

3.3.1 Electronic structure effects of BODIPY core alkylation

The effect of substitution on the BODIPY core was investigated in previous studies on BODIPY-anthracene dyads bearing different numbers of alkyl substituents [15]. Upon substitution, the HOMO energy increases gradually, while the HOMO–LUMO gap steadily decreases because the

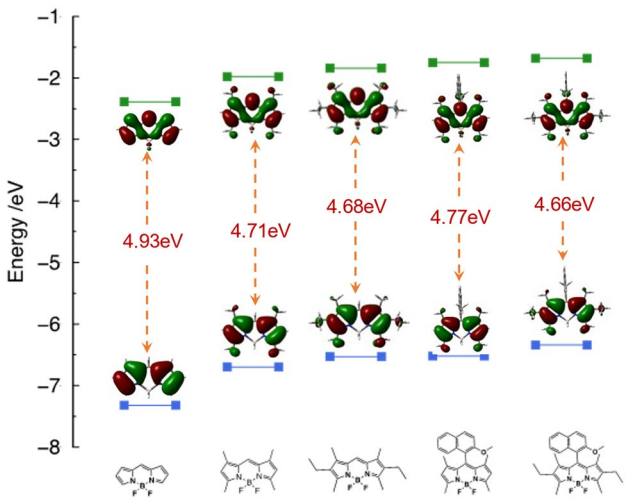

Fig. 4 Shapes and energies of HOMO (blue) and LUMO (green) of BODIPY and its derivatives calculated at M06-2X/6-311G* level at the ground state optimized geometry

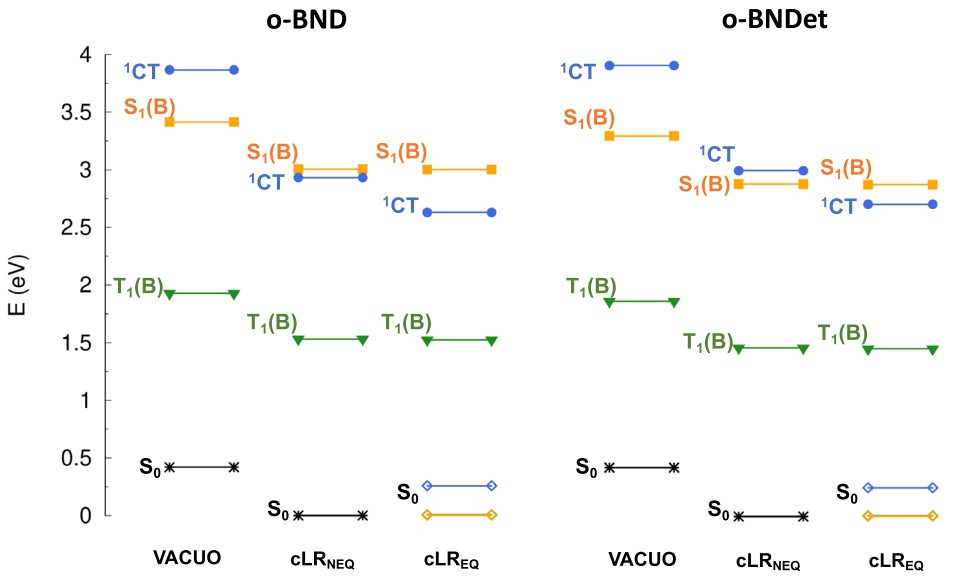

Fig. 5 Relevant excited states pattern of **o-BND** and **o-BNDet** calculated at the ground state geometry in vacuo and in MeCN (solvent effects described with the cLR scheme). The energy of S_0 is destabilized or stabilized accordingly. Note that in the cLR_{EQ} scheme, the S_0 energy is also state dependent and the color codes of S_0 cLR_{EQ} reflect the excited state on which the solvent is equilibrated

destabilization of the LUMO is more limited. Our results reveal a similar trend: in Fig. 4 we compare the computed orbital energies of **o-BND**, **o-BNDet**, with those of the simple BODIPY and its alkylated derivatives. The orbital energy trends change as expected, and as a result **o-BNDet** is characterized by a lower HOMO–LUMO gap compared to **o-BND**. Such reduced energy gap is expected to be reflected in a red-shifted maximum in the absorption spectrum of **o-BNDet** since the main band in the absorption spectrum is due to the excited state dominated by the HOMO–LUMO excitation (Table S2).

Accurate computational predictions of redox potentials require comparison of energies for both the starting molecule and its reduced/oxidized forms. However, we can qualitatively use Koopmans' theorem [59] to correlate the redox potentials of BODIPY dyads with HOMO/LUMO computed energies (Table S1). Compared to **o-BND,** the higher HOMO energy of **o-BNDet** implies an easier oxidation, in agreement with its lower oxidation potential. Similarly, the additional alkyl groups in the BODIPY core determine a higher LUMO energy which implies a lower tendency to be reduced in very good agreement with the experimental observation. Since the LUMO is localized on the BODIPY core, its increased energy in **o-BNDet** implies a reduced efficiency as electron acceptor which is expected to be reflected in higher lying charge transfer excited states in the ethylated dyad.

3.3.2 Low-lying excited states of BODIPY dyads

To discuss the efficiency of deactivation pathways for the two BODIPY derivatives, we determined the most relevant excitation energies and excited state wavefunctions in vacuo and including solvent effects, at the optimized ground state geometries (Table S2). As expected, among lowest-lying excited states we find the T_1(B) and S_1(B) states, dominated by the HOMO→LUMO excitation, localized on the BODIPY core. In addition, the two CT states ^{1}CT, ^{3}CT, almost degenerate are easily identified from computed results, due the localized nature of the frontier molecular orbitals (Figure S11) at the optimized ground state geometry of the two dyads, characterized by an almost perfect orthogonality of the donor with respect to the BODIPY core (Figure S1 and S2).

The quality of predicted excited states can be assessed by comparing the computed excitation energies in MeCN of **o-BND** to **o-BNDet**, with the experimental absorption spectra. To this end, we can consider three levels of solvent corrections, LR_{NEQ}, cLR_{NEQ} and cLR^2_{NEQ} on predicted excitation energies of the BODIPY localized lowest singlet excited state S_1(B), characterized by a large oscillator strength (Table S2), the state responsible for the main absorption band. The observed red shift of the main absorption band in **o-BNDet** compared to **o-BND**, is directly related with the reduced HOMO/LUMO gap of the former and is nicely reproduced by the calculations (Figure S12) at all levels of solvent correction. Disregarding the well-known overestimate of computed excitation energies at TD-DFT level [45–47] described in Sect. 2.2, we note that the red shift from **o-BND** to **o-BNDet** is predicted to be 0.11, 0.13 and 0.11 eV from $LR_{NEQ,}$ cLR_{NEQ} and cLR^2_{NEQ} calculations, respectively, in excellent agreement with experimental results in MeCN, showing a bathochromic shift of 0.12 eV.

The stabilization of the ^{1}CT singlet state, with respect to the BODIPY centered S_1(B) state, depends on alkyl substitution and on the environment, as expected given the large, computed, dipole moment of the charge separated state (Table S3). Both effects are crucial for the efficiency of the photoinduced processes, but solvent stabilization

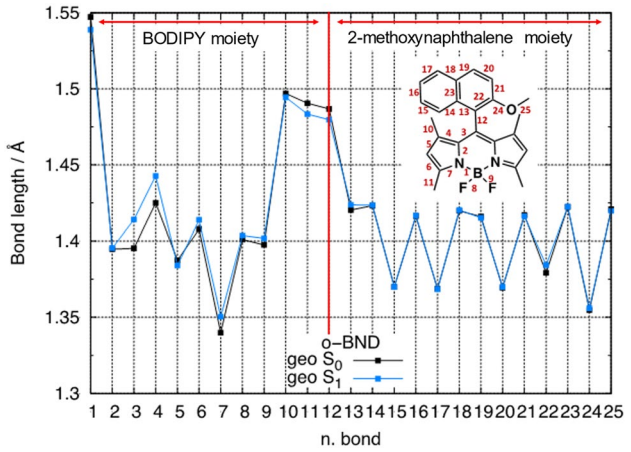

Fig. 6 Comparison between the bond lengths of **o-BND** in its ground and S_1(B) electronic states. From M06-2X/6-311G* calculations in MeCN

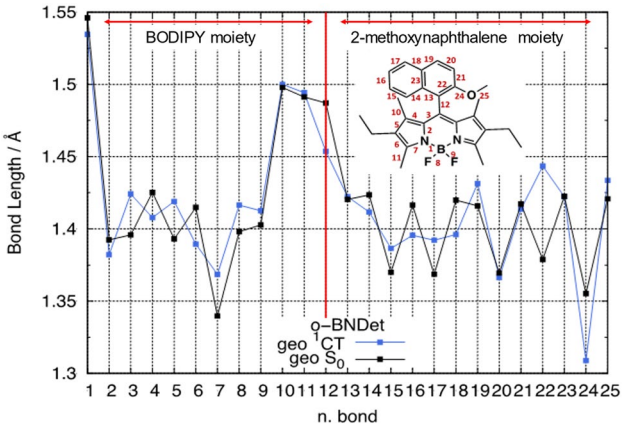

Fig. 7 Comparison between the bond lengths of **o-BNDet** in its ground S_0 and excited ^{1}CT electronic states. From M06-2X/6-311G* calculations in MeCN

is also influenced by the timescale of the photoinduced process, which may or may not allow full solvent equilibration. To get some insight on the magnitude of solvent stabilization associated with different timescales, in addition to the already discussed calculations of solvent effects with the fast solvent component equilibrated (LR_{NEQ} and cLR_{NEQ}) we also determined the relevant low-lying excited states including fully equilibrated solvent effects (LR_{EQ} and cLR_{EQ} schemes). These calculations show remarkably different results for **o-BND** and **o-BNDet** (Figs. 5 and S13). Specifically, the ^{1}CT state is predicted above S_1(B) in vacuo for both dyads, while in MeCN a remarkable stabilization occurs. With only the fast solvent component equilibrated, (cLR_{NEQ} calculations) the ^{1}CT gets closer to S_1(B) for **o-BNDet** and becomes the lowest singlet for **o-BND.** Finally, with solvent fully equilibrated in the excited state (cLR_{EQ} predictions) the ^{1}CT state drops below the S_1(B) state for both dyads, although it remains closer to the S_1(B) state for **o-BNDet** (0.17 eV), compared to **o-BND** (0.37 eV). The lower stabilization of the ^{1}CT state for **o-BNDet** can be traced back to the alkyl substituent effect.

The optimized S_1(B) geometry (Figure S3) clearly reflects the localized character of the BODIPY centered excitation as can be seen in Fig. 6, showing modest bond length changes localized only on the BODIPY core. Interestingly, the donor is not perfectly perpendicular to the BODIPY core and the S_1(B) equilibrium structure is characterized by a deviation from orthogonality of the naphthyl substituent, with a change of the dihedral angle from ca. 91° in the ground state to ca. 72° (Table S4). Notably, the relative energy order of low-lying excited states (Figure S14) is very similar to what has been discussed for the ground state geometry: the ^{1}CT state of both dyads

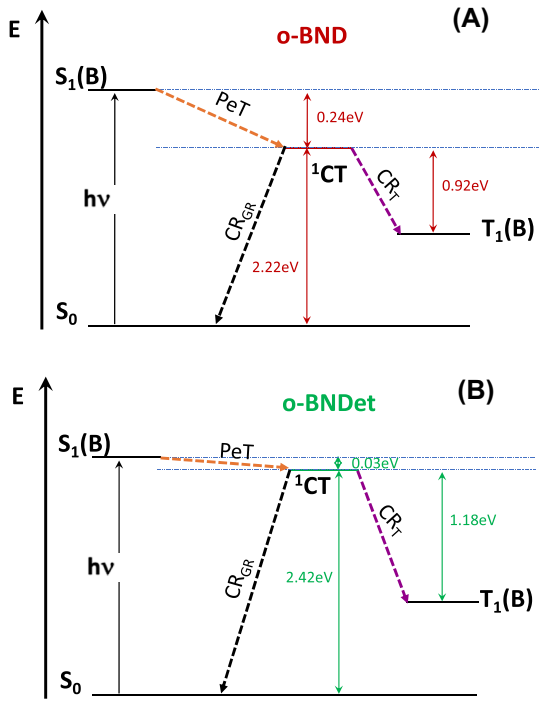

Fig. 8 Schematic representation of the three deactivation processes: PeT, CR_{GR} and CR_T in **a o-BND** and **b o-BNDet**, from computed excited state energies (TD-M06-2X/6-311G* level, including cLR_{EQ} solvent corrections)

becomes the lowest singlet excited state for fully equilibrated solvent but its stabilization is larger (0.24 eV below S_1(B)) for **o-BND** compared to **o-BNDet** (0.03 eV below S_1(B)).

As discussed in Sect. 2.2, due to the limits of the LR method, the ^{1}CT equilibrium geometry was determined only for **o-BNDet**. Its comparison with the ground state geometry shows clear traces of the electron transfer character since

both the donor and the acceptor moieties are subject to substantial bond length changes (Fig. 7). Similar bond length changes are determined for the ^{3}CT equilibrium structure (Figure S15) which, therefore can be taken as an acceptable representation of the ^{1}CT state for **o-BND**.

3.3.3 Efficiency of $S_1(B) \rightarrow {}^1CT$, $^1CT \rightarrow S_0$ and SOCT-ISC deactivations

According to the excited state stabilizations investigated in the previous section, we can discuss the deactivation processes following excited state population. Based on the present and previous experimental investigations on similar BODIPY dyads [24], the internal conversion taking place in $S_1(B)$ to generate the ^{1}CT state, is expected to be fast but the timescales of solvent reorganization [60] (picosecond, sub-picosecond [60]) are faster, such that we can discuss this process (schematically depicted in Fig. 8) assuming solvent equilibrated excited state energies (from cLR_{EQ} calculations) at the equilibrium $S_1(B)$ geometry (Figure S14, Table S5). For both molecules, the ^{1}CT state is more stable than the $S_1(B)$ state: $\Delta E(^1CT/S_1(B))$ is −0.24 eV for **o-BND** and −0.03 eV for **o-BNDet**. Our computed $\Delta E(^1CT/S_1(B))$ energy differences compare qualitatively well with the ΔG^0 values of this deactivation process, previously reported for similar dyads [24]. We note that the energy difference predicted for **o-BNDet** is less than one kcal/mol which, on one hand implies a non-negligible population of the $S_1(B)$ fluorescent state and on the other hand is probably smaller that the error of the method. Thus, we cannot rule out that the ^{1}CT state is indeed above $S_1(B)$ for **o-BNDet**. Accordingly, we can conclude that the rate constant associated with PeT is expected to be considerably larger for **o-BND** compared to **o-BNDet**, owing to the larger stability of the ^{1}CT state. The predicted inefficient formation of the ^{1}CT state for **o-BNDet** is in agreement with its predominant fluorescence deactivation.

The two major deactivation pathways of the ^{1}CT state are $^1CT \rightarrow S_0$ and $^1CT \rightarrow T_1(B)$. The CR_{GR} is expected to be slow because of the large $\Delta E(^1CT/S_0)$ energy difference, falling in the Marcus inverted region. Thus, solvent equilibrated energies (cLR_{EQ}) computed at the CT state geometry (Table S5) are considered for this process (also shown schematically in Fig. 8). Because the $\Delta E(^1CT/S_0)$ is slightly larger for **o-BNDet** compared to **o-BND**, the CR_{GR} processes is expected to be slightly less efficient for the former. Thus, the PeT is more favored for **o-BND**, while CR_{GR} is expected to be inefficient for both dyads although slightly more efficient for **o-BND**.

The other competing deactivation pathway, the formation of the $T_1(B)$ state via SOCT-ISC, due to the typical magnitude of the SOC integrals (ca. 1 cm^{-1}), is also a slow process [24] (of the order of 10^7–10^8 s^{-1}) compared to typical timescales of solvent reorganization [60]. Thus, solvent-equilibrated excited state energy differences (cLR_{EQ} values, see Table S5) and computed SOC integrals are employed to discuss the efficiency of this process. The SOC integrals between the ^{1}CT and $T_1(B)$ states, computed at two different geometries (ground state and CT, see Table 3) are in line with the typical values above, and also agree with those deduced for other BODIPY dyads [24]. Notably, although the two geometries (optimized ground and CT states) display different degrees of orthogonality between the naphthyl substituent and the BODIPY core, both consistently suggest a similar decay pattern, with the computed SOCs larger for **o-BND** compared to **o-BNDet.** For radiationless transitions slower than vibrational relaxation [61], and for relatively large ΔE_{S-T} energy gaps, the ISC process can be discussed in terms of a simplified relation (Eq. 1), where the rate constant (k_{ISC}) is proportional to the SOC matrix element, $\langle T_1(B)|\widehat{H_{SO}}|^1CT\rangle$ in this case, and inversely proportional to the square of the energy gap ΔE_{S-T}, namely the $\Delta E(^1CT/T_1(B))$ values [61–64]:

$$k_{ISC} \propto \frac{\left|\langle T_1(B)|\widehat{H_{SO}}|^1CT\rangle\right|^2}{(\Delta E_{S-T})^2} \quad (1)$$

Since $\Delta E(^1CT/T_1(B))$ is smaller for **o-BND** (0.92 eV) with respect to **o-BNDet** (1.18 eV) at the CT state geometry (Fig. 8, Table S5), and the SOC is larger, both factors favor the ISC of **o-BND**. Notably, such predicted $\Delta E(^1CT/T_1(B))$ energy differences are in very good agreement with those reported for other similarly efficient dyads [24] ($\Delta E(^1CT/T_1(B))$ in the range 0.81–1.01 eV). Thus, calculations also predict a less efficient triplet generation for **o-BNDet** compared to **o-BND**.

Table 3 Computed SOC magnitudes between ^{1}CT and $T_1(B)$ for **o-BND** and **o-BNDet**

Molecule	Ground state geometry		CT state geometry	
	SOC (^{1}CT/$T_1(B)$) [cm^{-1}][a]	(ΔE_{S-T} [eV])[b]	SOC (^{1}CT/$T_1(B)$) [cm^{-1}][a]	(ΔE_{S-T} [eV])[b]
o-BND	0.64	1.10	1.35	0.92
o-BNDet	0.53	1.25	0.98 [0.98][c]	1.18 [1.07][c]

[a]SOC values calculated with the SOMF(1X) approach including relativistic corrections with ZORA, from TDA-M06-2X/ZORA-def2-TZVP calculations at M06-2X/6-311G* optimized geometries

[b]ΔE_{S-T} from TD-M06-2X/6-311G*, including cLR_{EQ} solvent correction

[c]The values in square parentheses were computed at the ^{1}CT optimized geometry. The remaining values were computed at the ^{3}CT optimized geometry

In summary, the computed relative stabilization of the ^{1}CT state in MeCN for the two dyads, crucially determines the efficiency of the two sequential processes $S_1(B) \rightarrow {}^1CT$ and SOCT-ISC, leading to the $T_1(B)$ state population. These are both predicted to be more efficient for **o-BND**, fully supporting the experimental evidence of preferential triplet state population for **o-BND**.

3.3.4 Intra-molecular and solvent reorganization energies.

The intramolecular reorganization energies λ_i associated with the three photoinduced events discussed above were computed for **o-BNDet**. Not surprisingly, for $S_1(B) \rightarrow {}^1CT$ PeT and CR_{GR} process, the computed values are similar (0.60 and 0.66 eV, respectively) since the two deactivation pathways involve very similar geometry changes. Indeed, the two processes share a common state (^{1}CT), but the S_0 and $S_1(B)$ states involved as the initial or final states, have already been shown to display very similar geometries (see Fig. 6). These computed values are in reasonable agreement with the λ_i of 0.37 eV deduced from the fitting of PeT and CR_{GR} experimental data, recently determined for a library of BODIPY dyads [24]. Such previously investigated set of BODIPY dyads included rather different donors and the smaller 0.37 eV value (compared to our predicted λ_i) may result from the average over rather different donor substituents. The reorganization energy computed for the CR_T process amounts to 0.87 eV, in good agreement with the 0.70 eV deduced from the same set of BODIPY dyads [24].

The effect of solvent can be assessed also by estimating solvent reorganization energy λ_s, associated with $S_0 \rightarrow X$ processes (where $X = S_1(B)$, ^{1}CT and $T_1(B)$ excited states). Larger values are expected for excited states featuring a dipole moment substantially different from the ground state, but computed values also depend on the scheme adopted to introduce solvent effects (Table S6). Solvent corrections described with the LR approach are strongly dependent on the transition dipole moment, which explains the large reorganization energy predicted for the $S_1(B)$ state (0.24 eV) and the almost negligible values computed for the ^{1}CT and $T_1(B)$ states. In contrast, the SS cLR scheme predicts the largest reorganization energy for the CT state (0.56 eV at the S_0 geometry), as expected due to its large dipole moment compared to the ground state (Table S3). The most remarkable difference between predicted cLR and cLR^2 contributions is found for the $S_1(B)$ state (0.01 and 0.25 eV, respectively), and can be traced back to the influence of the LR term (namely the solvent response through the transition density) to the cLR^2 correction [39, 65]. When moving from the ground state geometry to the $S_1(B)$ geometry, the computed solvent reorganization energies undergo modest changes (Table S6) in agreement with the modest S_0–$S_1(B)$ geometry change. In contrast, the computed equilibrium structures of the CT state imply rather remarkable geometry changes and are accompanied by a mixing of the $S_1(B)$ and CT character. This is reflected in remarkably different computed λ_s values for the $S_0 \rightarrow S_1(B)$ and $S_0 \rightarrow {}^1CT$ processes, with the latter generally reduced and the former increased. The computed reorganization energy of the $S_0 \rightarrow {}^1CT$ process can be directly compared with the solvent reorganization deduced for the CR_{GR} process by fitting experimental data on a series of BODIPY dyads [24], which is reported to be 0.17 eV. Such value is considerably smaller compared to our computed values of 0.56 eV (**o-BND**) and 0.54 eV (**o-BNDet**) at the ground state geometry or 0.49 eV (**o-BND**) and 0.45 eV (**o-BNDet**) at the optimized S_1 geometry. Interestingly, however, the λ_s computed at the equilibrium structure of the ^{1}CT state, the most appropriate geometry to discuss the CR_{GR} process, range between 0.13 and 0.17 eV with the latter (obtained with the cLR^2 scheme) perfectly matching the experimentally deduced value. These results further support the reliability of solvent corrections introduced in our calculations to describe the photo-induced processes in these BODIPY dyads.

4 Conclusion

In this work, we rationalized the efficiency of CT-mediated triplet state generation in two BODIPY dyads featuring a methoxy-naphthalene donor covalently linked in the *meso*-position of the BODIPY core with different alkyl substituents, by combining an experimental photophysical and electrochemical investigation with computational studies of the relevant photo-induced processes.

The photophysical measurements indicated that the CT-state-mediated mechanism that leads to the population of $T_1(B)$ is viable in **o-BND**, but not in the case of **o-BNDet**, the latter showing a significantly higher fluorescence quantum yield.

To assess the effects of solvent and ethyl substitution on the sequence of photoinduced events, DFT and TD-DFT calculations were carried out including different solvent correction schemes. We found that $LR_{NEQ,}$ cLR_{NEQ} and $cLR^2{}_{NEQ}$ approaches predict, in MeCN, a red shift of the most intense absorption band of **o-BNDet** compared to **o-BND**, in excellent agreement with experimental data. To further assess the accuracy of the computed results, intramolecular and solvent reorganization energies associated with photo-induced processes were determined and showed to agree with values deduced by fitting photophysical data from a large set of BODIPY dyads.

Quantum-chemical calculations demonstrated that solvent equilibration in the excited states (cLR_{EQ} predictions) stabilizes the ^{1}CT state below the $S_1(B)$ state to a

different extent for the two dyads, with **o-BNDet** displaying a reduced stabilization compared to **o-BND** that can be traced back to the alkyl substituent effect. As a result, the $S_1(B) \rightarrow {}^1CT$ PeT in MeCN is predicted to be more efficient for **o-BND** compared to **o-BNDet** which supports the higher fluorescence of **o-BNDet**. The rate constant of the CR_{GR} process is expected to be small for both dyads due to the large energy gap between the S_0 and the ^1CT states falling in the inverted Marcus region. In contrast, a more efficient triplet state generation via SOCT-ISC is expected for **o-BND** thanks to a larger SOC and reduced $T_1(B)/{}^1CT$ energy gap. The predictions of more efficient PeT and CR_T processes for **o-BND** in MeCN fully support the experimental observation and demonstrate how alkyl substitution and solvent stabilization can crucially determine the outcome of photoinduced events.

Supplementary Information The online version contains supplementary material available at https://doi.org/10.1007/s43630-023-00530-1.

Funding Open access funding provided by Alma Mater Studiorum - Università di Bologna within the CRUI-CARE Agreement. The National PRIN 2017 projects (ID: 20174SYJAF, SURSUMCAT and ID: 20172M3K5N, CHIRALAB) is acknowledged for financial support for this research. Fondazione CarisBo is acknowledged for the funding of the project "Tecnologie avanzate per il controllo e lo sviluppo di molecole innovative per la salute" (ID: #18668). FN acknowledges support by the European Union—Next Generation EU under the Italian National Recovery and Resilience Plan (PNRR M4C2, Investimento 1.4—Avviso n. 3138 del 16/12/2021—CN00000013 National Centre for HPC, Big Data and Quantum Computing (HPC)—CUP J33C22001170001). PC acknowledges financial support from the National Recovery and Resilience Plan (NRRP), Mission 4 Component 2 Investment 1.3—Call for tender No. 1561 of 11.10.2022 of Ministero dell'Università e della Ricerca (MUR); funded by the European Union—NextGenerationEU.

Data availability Data are available on request from the authors.

Declarations

Conflict of interest The authors declare that they have no conflict of interest.

References

1. Romero, N. A., & Nicewicz, D. A. (2016). Organic photoredox catalysis. *Chemical Reviews, 116*, 10075–10166.
2. Shaw, M. H., Twilton, J., & MacMillan, D. W. C. (2016). Photoredox catalysis in organic chemistry. *Journal of Organic Chemistry, 81*, 6898–6926.
3. Glaser, F., & Wenger, O. S. (2020). Recent progress in the development of transition-metal based photoredox catalysts. *Coordination Chemistry Reviews, 405*, 213129.
4. Kwiatkowski, S., Knap, B., Przystupski, D., Saczko, J., Kędzierska, E., Knap-Czop, K., Kotlińska, J., Michel, O., Kotowski, K., & Kulbacka, J. (2018). Photodynamic therapy—Mechanisms, photosensitizers and combinations. *Biomedicine & Pharmacotherapy, 106*, 1098–1107.
5. Kamkaew, A., Lim, S. H., Lee, H. B., Kiew, L. V., Chung, L. Y., & Burgess, K. (2013). BODIPY dyes in photodynamic therapy. *Chemical Society Reviews, 42*, 77–88.
6. Callaghan, S., & Senge, M. O. (2018). The good, the bad, and the ugly-controlling singlet oxygen through design of photosensitizers and delivery systems for photodynamic therapy. *Photochemical & Photobiological Sciences, 17*, 1490–1514.
7. Bharmoria, P., Bildirir, H., & Moth-Poulsen, K. (2020). Triplet–triplet annihilation based near infrared to visible molecular photon upconversion. *Chemical Society Reviews, 49*, 6529–6554.
8. Castellano, F. N., & McCusker, C. E. (2015). MLCT sensitizers in photochemical upconversion: Past, present, and potential future directions. *Dalton Transactions, 44*, 17906–17910.
9. Zhou, J., Liu, Q., Feng, W., Sun, Y., & Li, F. (2015). Upconversion luminescent materials: Advances and applications. *Chemical Reviews, 115*, 395–465.
10. Bassan, E., Gualandi, A., Cozzi, P. G., & Ceroni, P. (2021). Design of BODIPY dyes as triplet photosensitizers: Electronic properties tailored for solar energy conversion, photoredox catalysis and photodynamic therapy. *Chemical Science, 12*, 6607–6628.
11. Zhao, J., Xu, K., Yang, W., Wang, Z., & Zhong, F. (2015). The triplet excited state of Bodipy: Formation, modulation and application. *Chemical Society Reviews, 44*, 8904–8939.
12. Bassan, E., Dai, Y., Fazzi, D., Gualandi, A., Cozzi, P. G., Negri, F., & Ceroni, P. (2022). Effect of the iodine atom position on the phosphorescence of BODIPY derivatives: A combined computational and experimental study. *Photochemical and Photobiological Sciences*. https://doi.org/10.1007/s43630-021-00152-5
13. Bassan, E., Calogero, F., Dai, Y., Dellai, A., Franceschinis, A., Pinosa, E., Negri, F., Gualandi, A., Ceroni, P., & Cozzi, P. G. (2023). Meso-2-methoxynaphthalenyl-BODIPY as efficient organic dye for metallaphotoredox catalysis. *ChemCatChem*. https://doi.org/10.1002/cctc.202201380
14. Filatov, M. A. (2020). Heavy-atom-free BODIPY photosensitizers with intersystem crossing mediated by intramolecular photoinduced electron transfer. *Organic & Biomolecular Chemistry, 18*, 10–27.
15. Filatov, M. A., Karuthedath, S., Polestshuk, P. M., Callaghan, S., Flanagan, K. J., Telitchko, M., Wiesner, T., Laquai, F., & Senge, M. O. (2018). Control of triplet state generation in heavy atom-free BODIPY-anthracene dyads by media polarity and structural factors. *Physical Chemistry Chemical Physics*. https://doi.org/10.1039/c7cp08472b
16. Mayländer, M., Quintes, T., Franz, M., Allonas, X., Vargas Jentzsch, A., & Richert, S. (2023). Distance dependence of enhanced intersystem crossing in BODIPY-nitroxide dyads. *Chemical Science*, 14, 5361–5368.
17. Ventura, B., Marconi, G., Bröring, M., Krüger, R., & Flamigni, L. (2009). Bis(BF 2)-2,2′-bidipyrrins, a class of BODIPY dyes with

new spectroscopic and photophysical properties. *New Journal of Chemistry, 33*, 428–438.
18. García-Moreno, I., Postils, V., Rebollar, E., Ortiz, M. J., Agarrabeitia, A. R., & Casanova, D. (2022). Generation of multiple triplet states in an orthogonal bodipy dimer: A breakthrough spectroscopic and theoretical approach. *Physical Chemistry Chemical Physics: PCCP, 24*, 5929–5938.
19. Sunahara, H., Urano, Y., Kojima, H., & Nagano, T. (2007). Design and synthesis of a library of BODIPY-based environmental polarity sensors utilizing photoinduced electron-transfer-controlled fluorescence ON/OFF switching. *Journal of the American Chemical Society, 129*, 5597–5604.
20. Magagnano, G., Gualandi, A., Marchini, M., Mengozzi, L., Ceroni, P., & Cozzi, P. G. (2017). Photocatalytic ATRA reaction promoted by iodo-Bodipy and sodium ascorbate. *Chemical Communications, 53*, 1591–1594.
21. Wang, Z., & Zhao, J. (2017). Bodipy-anthracene dyads as triplet photosensitizers: Effect of chromophore orientation on triplet-state formation efficiency and application in triplet-triplet annihilation upconversion. *Organic Letters, 19*, 4492–4495.
22. Wang, Z., Ivanov, M., Gao, Y., Bussotti, L., Foggi, P., Zhang, H., Russo, N., Dick, B., Zhao, J., Di Donato, M., Mazzone, G., Luo, L., & Fedin, M. (2020). Spin–orbit charge-transfer intersystem crossing (ISC) in compact electron donor–acceptor dyads: ISC mechanism and application as novel and potent photodynamic therapy reagents. *Chemistry: A European Journal, 26*, 1091–1102.
23. Kim, S., Zhou, Y., Tohnai, N., Nakatsuji, H., Matsusaki, M., Fujitsuka, M., Miyata, M., & Majima, T. (2018). Aggregation-induced singlet oxygen generation: Functional fluorophore and anthrylphenylene dyad self-assemblies. *Chemistry: A European Journal, 24*, 636–645.
24. Buck, J. T., Boudreau, A. M., DeCarmine, A., Wilson, R. W., Hampsey, J., & Mani, T. (2019). Spin-allowed transitions control the formation of triplet excited states in orthogonal donor–acceptor dyads. *Chem, 5*, 138–155.
25. Dong, Y., Sukhanov, A. A., Zhao, J., Elmali, A., Li, X., Dick, B., Karatay, A., & Voronkova, V. K. (2019). Spin–orbit charge-transfer intersystem crossing (SOCT-ISC) in Bodipy-phenoxazine dyads: Effect of chromophore orientation and conformation restriction on the photophysical properties. *Journal of Physical Chemistry C, 123*, 22793–22811.
26. Mikulchyk, T., Karuthedath, S., De Castro, C. S. P., Buglak, A. A., Sheehan, A., Wieder, A., Laquai, F., Naydenova, I., & Filatov, M. A. (2022). Charge transfer mediated triplet excited state formation in donor–acceptor–donor BODIPY: Application for recording of holographic structures in photopolymerizable glass. *Journal of Materials Chemistry C, 10*, 11588–11597.
27. Kiseleva, N., Filatov, M. A., Fischer, J. C., Kaiser, M., Jakoby, M., Busko, D., Howard, I. A., Richards, B. S., & Turshatov, A. (2022). BODIPY–pyrene donor–acceptor sensitizers for triplet–triplet annihilation upconversion: The impact of the BODIPY-core on upconversion efficiency. *Physical Chemistry Chemical Physics: PCCP, 24*, 3568–3578.
28. Liang, H., Sun, S., Zafar, M., Yuan, Z., Dong, Y., Ji, S., Huo, Y., De Li, M., & Zhao, J. (2020). Tuning the SOCT-ISC of bodipy based photosentizers by introducing different electron donating groups and its application in triplet-triplet-annihilation upconversion. *Dyes and Pigments, 173*, 108003.
29. Zhao, Y., Duan, R., Zhao, J., & Li, C. (2018). Spin-orbit charge transfer intersystem crossing in perylenemonoimide-phenothiazine compact electron donor–acceptor dyads. *Chemical Communications, 54*, 12329–12332.
30. Tsuga, Y., Katou, M., Kuwabara, S., Kanamori, T., Ogura, S., Okazaki, S., Ohtani, H., & Yuasa, H. (2019). A twist-assisted biphenyl photosensitizer passable through glucose channel. *Chemistry: An Asian Journal, 14*, 2067–2071.
31. Sartor, S. M., McCarthy, B. G., Pearson, R. M., Miyake, G. M., & Damrauer, N. H. (2018). Exploiting charge-transfer states for maximizing intersystem crossing yields in organic photoredox catalysts. *Journal of the American Chemical Society, 140*, 4778–4781.
32. Zhao, Y., Li, X., Wang, Z., Yang, W., Chen, K., Zhao, J., & Gurzadyan, G. G. (2018). Precise control of the electronic coupling magnitude between the electron donor and acceptor in perylenebisimide derivatives via conformation restriction and its effect on photophysical properties. *Journal of Physical Chemistry C, 122*, 3756–3772.
33. Rehmat, N., Kurganskii, I. V., Mahmood, Z., Guan, Q. L., Zhao, J., Xing, Y. H., Gurzadyan, G. G., & Fedin, M. V. (2021). Spin–orbit charge-transfer intersystem crossing in anthracene–perylenebisimide compact electron donor–acceptor dyads and triads and photochemical dianion formation. *Chemistry: A European Journal, 27*, 5521–5535.
34. Grampp, G. (1993). The Marcus Inverted Region from theory to experiment. *Angewandte Chemie International Edition in English, 32*, 691–693.
35. Nepomnyashchii, A. B., & Bard, A. J. (2012). Electrochemistry and electrogenerated chemiluminescence of BODIPY dyes. *Accounts of Chemical Research, 45*, 1844–1853.
36. Tomasi, J., Mennucci, B., & Cammi, R. (2005). Quantum mechanical continuum solvation models. *Chemical Reviews, 105*, 2999–3093.
37. Mennucci, B. (2015). Modeling absorption and fluorescence solvatochromism with QM/classical approaches. *International Journal of Quantum Chemistry, 115*, 1202–1208.
38. Caricato, M., Mennucci, B., Tomasi, J., Ingrosso, F., Cammi, R., Corni, S., & Scalmani, G. (2006). Formation and relaxation of excited states in solution: A new time dependent polarizable continuum model based on time dependent density functional theory. *The Journal of Chemical Physics, 124*, 124520.
39. Guido, C. A., Chrayteh, A., Scalmani, G., Mennucci, B., & Jacquemin, D. (2021). Simple protocol for capturing both linear-response and state-specific effects in excited-state calculations with continuum solvation models. *Journal of Chemical Theory and Computation, 17*, 5155–5164.
40. Crosby, G. A., & Demas, J. N. (1971). Measurement of photoluminescence quantum yields. Review. *The Journal of Physical Chemistry A, 75*, 991–1024.
41. Montalti, M., Credi, A., Prodi, L., & Gandolfi, M. T. (2006). Handbook of photochemistry (3rd ed.). CRC Press.
42. Wilkinson, F., Helman, W. P., & Ross, A. B. (1993). Quantum yields for the photosensitized formation of the lowest electronically excited singlet state of molecular oxygen in solution. *Journal of Physical and Chemical Reference Data, 22*, 113–262.
43. Rio, Y., Accorsi, G., Nierengarten, H., Bourgogne, C., Strub, J.-M., Van Dorsselaer, A., Armaroli, N., & Nierengarten, J.-F. (2003). A fullerene core to probe dendritic shielding effects. *Tetrahedron, 59*, 3833–3844.
44. Chibani, S., Charaf-Eddin, A., Le Guennic, B., & Jacquemin, D. (2013). Boranil and related NBO dyes: Insights from theory. *Journal of Chemical Theory and Computation, 9*, 3127–3135.
45. Postils, V., Ruipérez, F., & Casanova, D. (2021). Mild open-shell character of BODIPY and its impact on singlet and triplet excitation energies. *Journal of Chemical Theory and Computation, 17*, 5825–5838.
46. Zinna, F., Bruhn, T., Guido, C. A., Ahrens, J., Bröring, M., Di Bari, L., & Pescitelli, G. (2016). Circularly polarized luminescence from axially chiral BODIPY DYEmers: An experimental and computational study. *Chemistry: A European Journal, 22*, 16089–16098.
47. Chibani, S., Laurent, A. D., Le Guennic, B., & Jacquemin, D. (2014). Improving the accuracy of excited-state simulations of

BODIPY and aza-BODIPY dyes with a joint SOS-CIS(D) and TD-DFT approach. *Journal of Chemical Theory and Computation, 10*, 4574–4582.
48. Chibani, S., Le Guennic, B., Charaf-Eddin, A., Laurent, A. D., & Jacquemin, D. (2013). Revisiting the optical signatures of BODIPY with ab initio tools. *Chemical Science, 4*, 1950–1963.
49. Charaf-Eddin, A., Le Guennic, B., & Jacquemin, D. (2014). Excited-states of BODIPY-cyanines: Ultimate TD-DFT challenges? *RSC Advances, 4*, 49449–49456.
50. Laine, M., Barbosa, N. A., Wieczorek, R., Melnikov, M. Y., & Filarowski, A. (2016). Calculations of BODIPY dyes in the ground and excited states using the M06-2X and PBE0 functionals. *Journal of Molecular Modeling*. https://doi.org/10.1007/s00894-016-3108-8
51. Chibani, S., Laurent, A. D., Blondel, A., Mennucci, B., & Jacquemin, D. (2014). Excited-state geometries of solvated molecules: Going beyond the linear-response polarizable continuum model. *Journal of Chemical Theory and Computation, 10*, 1848–1851.
52. Nelsen, S. F., Blackstock, S. C., & Kim, Y. (1987). Estimation of inner shell Marcus terms for amino nitrogen compounds by molecular orbital calculations. *Journal of the American Chemical Society, 109*, 677–682.
53. Frisch, M. J., Trucks, G. W., Schlegel, H. B., Scuseria, G. E., Robb, M. A., Cheeseman, J. R., Scalmani, G., Barone, V., Petersson, G. A., Nakatsuji, H., Li, X., Caricato, M., Marenich, A. V., Bloino, J., Janesko, B. G., Gomperts, R., Mennucci, B., Hratchian, H. P., Ortiz, J. V., Izmaylov, A. F., Sonnenberg, J. L., Williams-Young, D., Ding, F., Lipparini, F., Egidi, F., Goings, J., Peng, B., Petrone, A., Henderson, T., Ranasinghe, D., Zakrzewski, J., Gao, V. G., Rega, N., Zheng, G., Liang, W., Hada, M., Ehara, M., Toyota, K., Fukuda, R., Hasegawa, J., Ishida, M., Nakajima, T., Honda, Y., Kitao, O., Nakai, H., Vreven, T., Throssell, K., Montgomery, J., A, J., Peralta, J. E., Ogliaro, F., Bearpark, M. J., Heyd, J. J., Brothers, E. N., Kudin, K. N., Staroverov, V. N., Keith, T. A., Kobayashi, R., Normand, J., Raghavachari, K., Rendell, A. P., Burant, J. C., Iyengar, S. S., Tomasi, J., Cossi, M., Millam, J. M., Klene, M., Adamo, C., Cammi, R., Ochterski, J. W., Martin, R. L., Morokuma, K., Farkas, O., Foresman, J. B., & Fox, D. J. (2016). Gaussian, Inc.
54. De Souza, B., Farias, G., Neese, F., & Izsák, R. (2019). Predicting phosphorescence rates of light organic molecules using time-dependent density functional theory and the path integral approach to dynamics. *Journal of Chemical Theory and Computation, 15*, 1896–1904.
55. Neese, F. (2005). Efficient and accurate approximations to the molecular spin-orbit coupling operator and their use in molecular g-tensor calculations. *The Journal of Chemical Physics*. https://doi.org/10.1063/1.1829047
56. van Lenthe, E., Snijders, J. G., & Baerends, E. J. (1996). The zero-order regular approximation for relativistic effects: The effect of spin–orbit coupling in closed shell molecules. *The Journal of Chemical Physics, 105*, 6505–6516.
57. Neese, F., Wennmohs, F., Becker, U., & Riplinger, C. (2020). The ORCA quantum chemistry program package. *The Journal of Chemical Physics*. https://doi.org/10.1063/5.0004608
58. Hirata, S., & Head-Gordon, M. (1999). Time-dependent density functional theory within the Tamm–Dancoff approximation. *Chemical Physics Letters, 314*, 291–299.
59. Koopmans, T. (1934). Über die Zuordnung von Wellenfunktionen und Eigenwerten zu den Einzelnen Elektronen Eines Atoms. *Physica, 1*, 104–113.
60. Park, S., Kim, J., Moran, A. M., & Scherer, N. F. (2011). Solvent structural relaxation dynamics in dipolar solvation studied by resonant pump polarizability response spectroscopy. *Physical Chemistry Chemical Physics: PCCP, 13*, 214–223.
61. Plotnikov, V. G. (1979). Regularities of the processes of radiationless conversion in polyatomic molecules. *International Journal of Quantum Chemistry, 16*, 527–541.
62. Chen, Y.-L., Li, S.-W., Chi, Y., Cheng, Y.-M., Pu, S.-C., Yeh, Y.-S., & Chou, P.-T. (2005). Switching luminescent properties in osmium-based β-diketonate complexes. *ChemPhysChem, 6*, 2012–2017.
63. Zhang, J., Mukamel, S., & Jiang, J. (2020). Aggregation-induced intersystem crossing: Rational design for phosphorescence manipulation. *The Journal of Physical Chemistry B, 124*, 2238–2244.
64. Dong, Y., Kumar, P., Maity, P., Kurganskii, I., Li, S., Elmali, A., Zhao, J., Escudero, D., Wu, H., Karatay, A., Mohammed, O. F., & Fedin, M. (2021). Twisted BODIPY derivative: Intersystem crossing, electron spin polarization and application as a novel photodynamic therapy reagent. *Physical Chemistry Chemical Physics: PCCP, 23*, 8641–8652.
65. Knysh, I., Duchemin, I., Blase, X., & Jacquemin, D. (2022). Modeling of excited state potential energy surfaces with the Bethe–Salpeter equation formalism: The 4-(dimethylamino)benzonitrile twist. *The Journal of Chemical Physics, 157*, 194102.